A Novel Parallel All-Digital Buffered Telemetry Demodulator for Future Low Cost Space Missions*

H. Tsou, B. Shah, R. Lee and S. Hinedi

Jet Propulsion Laboratory
California Institute of Technology
4800 Oak Grove Drive, MS 238-343
Pasadena, CA 91109

July 22, 1993

Abstract

This paper functionally describes a novel Buffered Telemetry Demodulator (BTD) suitable for future low cost space missions characterized by low data rates and relatively weak space to ground communication links. The BTD operates on recorded (or buffered) digital samples to extract symbols from the received signal. It is more useful when the downlink margin is so low that signal acquisition takes an unusually long time and tracking loops frequently slip cycles. The key features of the BTD are (1) its ability to reprocess the signal to reduce acquisition time and enable resynchronization, (2) its ability to use future information about the signal and perform smoothing in the past to recover symbols lost during acquisition and resynchronization, (3) its minimized recording bandwidth as each harmonic of a square wave subcarrier is recorded individually, and (4) its parallel architecture that enables a multi-processor implementation. This paper also discusses the computational speed required to implement the BTD in software and identifies various general purpose computers that can be used for implementation.

1 Introduction

Changes in national policy are rapidly bringing the era of billion dollar deep space missions to an end. Due to constraints on total (design and operation) cost, future spacecrafts will

---

*The research described in this paper was carried out by the Jet Propulsion Laboratory, California Institute of Technology, under a contract with the National Aeronautics and Space Administration.

1

be characterized by smaller size and simpler designs. Consequently, future missions will be characterized by "low" data rates and relatively "weak" space-to-ground links. As a result, data compression techniques aboard the spacecraft and advanced signal processing techniques on the ground provide cheap alternatives to increase the scientific return of a mission by improving the communication link margin. This article functionally describes a novel Buffered Telemetry Demodulator (BTD) suitable for space missions characterized by low data rates, and relatively weak space-to-ground communication links. The BTD operates on recorded (or buffered) digital samples to extract symbols from the received signal. It is most useful when the downlink margin is so low that signal acquisition takes an unusually long time and tracking loops frequently slip cycles. The key features of the BTD are its ability to reprocess the signal to reduce acquisition time and enable resynchronization, (2) its ability to use future information about the signal and perform smoothing, in the past as recover symbols lost during acquisition and resynchronization, (3) its minimized recording bandwidth as each harmonic of a square wave subcarrier is recorded individually, and (4) its parallel architecture that enables a multi-processor implementation. The computational speed required to implement the BTD in software is also discussed and various general purpose computers that can be used for implementation are identified.

The applications of the BTD extend to current missions to provide emergency backup to operate the communication link below the threshold of current receivers. For example, consider NASA's Galileo spacecraft currently on its way to Jupiter. Due to mechanical problems that have rendered the Galileo spacecraft's high gain antenna unusable, the mission will have to rely on Galileo's low gain antenna for data transmission back to earth. The symbol rate for this low gain mission will vary from 32 sps (symbols per second) to 512 sps with symbol signal to noise ratios (SNRs) ranging from -10 dB to -6 dB. The link margin at these SNRs is so low that signal acquisition (carrier, subcarrier, and symbol) can take up to twenty minutes, resulting in significant data loss. In order to maximize the data rate, suppressed carriers are used and since the Costas loop SNR is a nonlinear function of the

symbol SNR, significant squaring loss results in the loop. Additionally, since the downlink symbol rate can be programmed to take advantage of the antenna apertures on the ground, several data rate changes can occur in a pass or a single day, each resulting in data loss due to resynchronization in the ground receiver. At present, data lost during acquisition or cycle slips is not recoverable because existing receivers in NASA's Deep Space Network (DSN) process the signal in real-time and do not buffer or store the received signal for reprocessing.

The Buffered Telemetry Demodulator (BTD) is a coherent receiving system which overcomes these problems by recording the signal and then processing and reprocessing the samples. Once acquisition occurs, the BTD can operate on the past data using estimates of the signal state (such as phase, frequency and (ID) bit rate) to basically go back in time and recover those symbols lost during acquisition. This is referred to as *smoothing* where future data is used to provide an estimate in the past. The BTD is designed mainly for low symbol rate applications and can be implemented on a general purpose workstation. In order to reduce the computational requirement, the signal is received on a subcarrier harmonic basis, thus rendering the BTD independent of the subcarrier frequency. This results in a computational throughput requirement based on the symbol rate rather than on the bandwidth of the transmitted signal. Consequently, when antenna arraying is employed [4], only a fraction of the total signal bandwidth needs to be transmitted between antenna sites resulting in significant reduction in transmission requirements.

Section 2 of this paper briefly reviews the existing coherent receiver which demodulates the downlink signal in real time. Sections 3 and 4 describe the recording and demodulation functions of the BTD. It is shown that the BTD performance exceeds that of existing receivers since no data is lost due to reprocessing. The BTD implementation on various workstations is evaluated in section 5, and smoothing strategies are discussed in section 6.

3

2 A Review of Current Receivers

In deep space communications, baseband symbols are typically first modulated onto a square-wave subcarrier and then onto a sine-wave carrier. This allows transmission of a residual carrier component whose frequency does not coincide with the data spectrum. Consequently, at the receiving end the deep space signal is demodulated using a carrier, subcarrier, and symbol synchronizer loop. This section briefly reviews the Advanced Receiver (ARX) [1] carrier and subcarrier loops so that they can be compared to the carrier and subcarrier loops of the BTD. The ARX is a receiving system that has been developed to digitally demodulate and process signals from deep space spacecraft. It is a breadboard system for the Block V receiver, which will eventually replace various receivers currently used in the DSN [2]. The main difference between the ARX and BTD is that the ARX carrier and subcarrier loops process the received signal after it has been open-loop down converted to an intermediate frequency (IF) process, the BTD loops process the received signal after it has been open-loop downconverted to baseband on a subcarrier harmonic basis. All the other receiving functions, e.g. symbol synchronization, symbol detection, lock detection, etc., are implemented the same way in both the ARX and BTD. Consequently, they are not discussed in this article. Instead, the interested reader is referred to [1] for a complete review of these functions.

A block diagram of the ARX carrier and subcarrier loops is shown in Fig. 1. The received signal, which is assumed to be a typical deep space signal, after downconversion to an appropriate IF can be represented as [2]

$$ r(t) = \sqrt{2P}\cos(\Lambda)\sin[\Psi_c(t)] + \sqrt{2P}\sin(\Lambda)d(t)\,\text{sgn}\{\sin[\Psi_{su}(t)]\}\cos[\Psi_c(t)] + n(t) \qquad (1) $$

where the first term represents the residual carrier component and the second term represents the data modulation. The total power P in Watts (W) is divided between the residual carrier and data by controlling the modulation index, Λ. Specifically, the carrier power $P_c = P\cos^2(\Lambda)$ and the data power $P_d = P\sin^2(\Lambda)$, respectively. The quantity $n(t)$ is the

total carrier phase and $\Psi_{su}(t)$ is the total subcarrier phase, both ill radians. The data, $d(t)$, is given by

$$d(t) = \sum_{l=-\infty}^{\infty} a_l p(t - lT) \tag{2}$$

where $p(t)$ is the unit-power square pulse limited to T seconds and $\{a_l\}$ represents the independent and equally likely binary (± 1) symbols. The noise process, $n(t)$, is modeled as bandpass with a flat one-sided power spectral density (PSD) level equal to N_0 W/Hz. By expressing the square-wave subcarrier as an infinite sum, i.e.,

$$\text{sgn}\{\sin[\Psi_{su}(t)]\} = \frac{4}{\pi} \sum_{\substack{j=1 \\ odd}}^{\infty} \frac{1}{j} \sin[j\Psi_{su}(t)] \tag{3}$$

the digitized signal which is sampled at rate $f_s = 1/T_s$ can be written as

$$r(kT_s) = \sqrt{2P_c} \sin[\Psi_c(kT_s)] + \sqrt{2P_d} d(kT_s) \left(\frac{4}{\pi} \sum_{\substack{j=1 \\ j \, odd}}^{L} \frac{\sin[j\Psi_{su}(kT_s)]}{j} \right) \cos[\Psi_c(kT_s)] + n(kT_s) \tag{4}$$

where only harmonics up to the Lth subcarrier harmonic (L is an odd integer) are assumed to be present at the A/D converter output in Fig. 2. Samples of the bandpass noise will be expressed as

$$n(kT_s) = \sqrt{2}n_1(kT_s) \cos[\Psi_c(kT_s)] - \sqrt{2}n_2(kT_s)\sin[\Psi_c(kT_s)] \tag{5}$$

where the random variables $n_1(kT_s)$ and $n_2(kT_s)$ are samples of the baseband noise processes $n_1(t)$ and $n_2(t)$ which are assumed to be statistically independent, white Gaussian noise processes with a flat one-sided PSD level equal to N_0 W/Hz within a one-sided bandwidth equal to $1/(2T_s)$ Hz. As a result, $n_1(kT_s)$ and $n_2(kT_s)$ are zero mean with variance $o_{n_1}^2 = o_{n_2}^2 = N_0/(2T_s)$. When appropriate, the time index kT_s will be omitted from now on to allow a simpler notation

The residual carrier tracking loop control signal, U_q in Fig. 1, is derived by mixing the digitized IF signal with its carrier quadrature component, low-pass filtering the mixer output,

and then accumulating the filtered samples over the loop update interval. Mathematically,

$$U_q = \sqrt{P_c} \sin(\phi_c) + n_{U_q} \tag{6}$$

where ϕ_c is the carrier phase error, n_{U_q} is a zero mean Gaussian random variable with variance $N_0/(2T_u)$, and $T_u = M_1 T_s$ is the loop update interval in seconds. Note that the data has been neglected in writing (6), since it is assumed that the accumulator in the carrier quadrature arm averages over several subcarrier cycles (i. e., $f_{su}T_u \gg 1$) so that the data sum is approximately zero. It will be shown in section 4 that the BTD carrier loop control signal has the same signal power and noise statistics as (6) and therefore, both loops will have the same tracking performance.

Next, let's consider the subcarrier tracking loop. As shown in Fig. 1, the input to the subcarrier loop is the quadrature component of the residual carrier. The subcarrier control signal is obtained by forming the product $Z_i Z_{q,su}$ where Z_i is the output of the subcarrier in-phase arm and $Z_{q,su}$ is the output of the subcarrier quadrature arm. Note that the subscript 'su' in $Z_{q,su}$ is used to distinguish it from $Z_{q,sca}$, the quadrature arm of the suppressed carrier loop. The signals Z_i and $Z_{q,su}$, obtained after respectively mixing the residual carrier quadrature component with the subcarrier in-phase and quadrature references and then accumulating these samples over a symbol duration (perfect symbol synchronization assumed), are given as [1]

$$Z_i = \sqrt{P_d a_1} F_I(\phi_{su}) \cos(\phi_c) + n_{Z_i} \tag{7}$$

and

$$Z_{q,su} = \sqrt{P_d a_1} F_Q(\phi_{su}) \cos(\phi_c) + n_{Z_{q,su}} \tag{8}$$

where ϕ_{su} is the subcarrier phase error and the functions, $F_I(\phi_{su})$ and $F_Q(\phi_{su})$, are periodic functions of ϕ_{su} (period 2π) given in the principal phase interval $[-\pi, \pi]$ as follows [1]

$$F_I(\phi_{su}) = 1 - \frac{2}{\pi} |\phi_{su}|, \ |\phi_{su}| \le \pi \tag{9}$$

6

and

$$F_Q(\phi_{su}) , \begin{cases} (2/\pi)(\%3,(& |\phi_{su}| \le (\pi/2)W_{su} \\ \text{sgn}(\phi_{su})W_{su} & (\pi/2)W_{su} \le |\phi_{su}| < \pi(1 - W_{su}/2) \\ 2\text{sgn}(\phi_{su}) - (2/\pi)\phi_{su} & \pi(1 - W_{su}/2) \le |\phi_{su}| \le \pi \end{cases} \tag{1o}$$

The parameter W_{su}, ill fractions of cycles, is the width of the subcarrier window ($W_{su} \le 1$ and $W_{su} = 1$ corresponds to no window). It is used in the quadrature arm to improve the square-wave tracking performance [3]. The noise n_{Z_i} and $n_{Z_{q,su}}$ in (7) and (8) are independent with respective variances $N_0/(2T')$ and $N_0 W_{su}/(2'/')$ where T' denotes symbol duration. It will be shown in section 4 that the 1{ '1 '1) in-phase and quadrature accumulator outputs have the same signal and noise statistics as ('/) and (8). Consequently, both subcarrier loops will have the same control signal and therefore, the same tracking performance.

Finally, let's consider the suppressed carrier with subcarrier case ($A = 90°$ in (1)). In this scenario, the suppressed carrier loop control signal is obtained by forming the product $Z_i Z_{q,sca}$ as shown in Fig. 1. The signal Z_i, which was shown to be the subcarrier in-phase component, now becomes the suppressed carrier in-phase component because it is already proportional to $\cos(\phi_c)$ and $F_I(\phi_{su})$ as indicated by (7). The suppressed carrier quadrature component $Z_{q,sca}$ is generated by mixing the digitized IF signal with the quadrature carrier reference and the in-phase subcarrier reference, and then accumulating the resulting samples over a symbol duration. Hence, the suppressed carrier in-phase and quadrature signals are given as [1]

$$Z_i = \sqrt{P_d a_1} F_I(\phi_{su}) \cos(\phi_c) + n_{Z_i} \tag{11}$$

and

$$Z_{q,sca} = \sqrt{P_d a_1} F_I(\phi_{su}) \sin(\phi_c) + n_{Z_{q,sca}} \tag{12}$$

where n_{Z_i} and $n_{Z_{q,sca}}$ are independent with variance $N_0/(2T)$. It will be shown in section 4 that the in-phase and quadrature signals of the B TD suppressed carrier loop have the same statistics as in (1 1) and (1 2). Hence, both suppressed carrier loops will have the same error

sig, nal and tracking performance.

3   Baseband Recording

As indicated earlier, the BTD processes the received signal after it has been open-loop (lou'llc.oil\'(:Jt(:(l" to baseband on a subcarrier harmonic basis and recorded on tape. This section describes two methods for recording the received signal at baseband. The first recording scheme, depicted in Fig. 2a, distributes the sampled IF signal into 2 carrier channels and $4n$ subcarrier channels where n denotes the number of subcarrier harmonics present at the A/D output and is related to L (the highest recorded subcarrier harmonic) through $L = 2n - 1$. Recording of the carrier requires two channels because baseband demodulation requires both in-phase and quadrature samples. Similarly, recording of each subcarrier harmonic requires 4 channels, 2 channels (1 in-phase subcarrier channel and 1 quadrature subcarrier channel) per carrier channel (in-phase and quadrature). Table 1a depicts the loss in data power as a function of the highest recorded subcarrier harmonic L.

Each band of the sampled IF signal is recorded at baseband after mixing it with tones tuned to its predicted center frequency. The predicts are assumed to be close, but not exactly equal, to the actual band center frequency. For example, consider the two channels that record the residual carrier. In the residual carrier sine channel, the sampled IF signal is mixed with $\sqrt{2}\sin\hat{\Psi}_c(kT_s)$, where $\hat{\Psi}_c(kT_s)$ is an estimate of the actual carrier phase $\Psi_c(kT_s)$, and low-pass filtered to obtain the recorded waveform $C_s(kT_s)$. Similarly, in the residual carrier cosine channel, the sampled IF signal is mixed with $\sqrt{2}\cos\hat{\Psi}_c(kT_s)$ and low-pass filtered to obtain $C_c(kT_s)$. The recorded carrier is given by [6]

$$C_s = \sqrt{P_c}\cos(\Theta_c) + n_{c_s} \tag{13a}$$

$$C_c = \sqrt{P_c}\sin(\Theta_c) + n_{c_c} \tag{13b}$$

8

where $\Theta_c \overset{\Delta}{=} \Psi_c - \hat{\Psi}_c$, and where, using the Heaviside operator notation[1],

$$n_{c_s} = H_c(z) \{ - n_1 \sin(\Theta_c) - n_2 \cos(\Theta_c)\} \tag{14a}$$

$$n_{c_c} = H_c(z) \{ n_1 \cos(\Theta_c) - n_2 \sin(\Theta_c)\} \tag{14b}$$

The low-pass filter $H_c(z)$ is assumed to be bandlimited to B_c Hz. Furthermore, since the carrier frequency error (derivative of Θ_c) is assumed to be much smaller than B_c, both n_{c_c} and n_{c_s} are baseband processes limited to B_c with a flat one-sided PSD level equal to N_0 W/Hz.

One approach to baseband recording of the subcarrier is the two-stage downconversion scheme shown in Fig. 2a. The first stage centers the IF spectrum near dc by mixing it with sine and cosine references tuned to the predicted carrier frequency. The second stage first individually downconverts each of the subcarrier harmonics to baseband by mixing the output of the first stage with sine and cosine references tuned to multiples of the predicted subcarrier frequency, then low-pass filters the mixer output followed by recording of the desired subcarrier harmonic. The data power loss due to low-pass filtering is tabulated in Table 1 b as a function of the ratio of the bandwidth B_{su} (of the filter $H_{su}(z)$ in Fig. 2) to symbol rate.[2] As shown in section 4, coherent subcarrier demodulation requires an integer phase relationship be maintained between the subcarrier references that downconvert the subcarrier harmonics to baseband. That is, let $\hat{\Psi}_{su}$ denote the phase of the reference that downconverts the fundamental harmonic, then the mth subcarrier harmonic is downconverted by mixing the output of stage 1 with references that have phase equal to $m\hat{\Psi}_{su}$. The four signals corresponding to the recording of the mth subcarrier harmonic are represented as (m is an odd integer) [6]

$$SU_{ss}^{(m)} = \sqrt{P_d} \frac{2d}{\pi m} \cos[m\Theta_{su}]\sin(\Theta_c) + n_{SU_{ss}}^{(m)} \tag{15a}$$

[1] The Heaviside operation $H(z)\{x(m)\}$ denotes the convolution of $x(m)$ with $h(m)$, i.e. $H(z)\{x(m)\} \overset{\Delta}{=} \sum_{m=-\infty}^{m} x(n)h(m-n)$

[2] Loss in Table 1b is for an ideal lowpass filter with bandwidth B_{su} and given by $\int_{-mB_{su}}^{mB_{su}} \text{sinc}^2 fT\,df$

9

$$SU_{sc}^{(m)} = -\sqrt{P_d} \frac{2d}{\pi m} \sin[m\Theta_{su}] \sin(\Theta_c) + n_{SU_{sc}}^{(m)} \tag{15b}$$

$$SU_{cs}^{(m)} = +\sqrt{P_d} \frac{2d}{\pi m} \cos[m\Theta_{su}] \cos(\Theta_c) + n_{SU_{cs}}^{(m)} \tag{1D\Gamma}$$

$$SU_{cc}^{(m)} = +\sqrt{P_d} \frac{2d}{\pi m} \sin[m\Theta_{su}] \cos(\Theta_c) + n_{SU_{cc}}^{(m)} \tag{15d}$$

where the noise terms are given by

$$n_{SU_{ss}}^{(m)} = -H_{su}(z) \left\{ [n_1 \sin(\Theta_c) + n_2 \cos(\Theta_c)] \sin[m\hat{\Psi}_{su}] \right\} \tag{16a}$$

$$n_{SU_{sc}}^{(m)} = -H_{su}(z) \left\{ [n_1 \sin(\Theta_c) + n_2 \cos(\Theta_c)] \cos[m\hat{\Psi}_{su}] \right\} \tag{16b}$$

$$n_{SU_{cs}}^{(m)} = H_{su}(z) \left\{ [n_1 \cos(\Theta_c) - n_2 \sin(\Theta_c)] \sin[m\hat{\Psi}_{su}] \right\} \tag{16c}$$

$$n_{SU_{cc}}^{(m)} = H_{su}(z) \left\{ [n_1 \cos(\Theta_c) - n_2 \sin(\Theta_c)] \cos[m\hat{\Psi}_{su}] \right\} \tag{16d}$$

It can be verified that $n_{SU_{sc}}^{(m)}, n_{SU_{ss}}^{(m)}, n_{SU_{cc}}^{(m)},$ and $n_{SU_{cs}}^{(m)}$ are baseband processes limited to B_{su}, the bandwidth of the low-pass filter $H_{su}(z)$, with a flat ollc-sided PSD level equal to $N_0/2$ W/Hz. Moreover, it can be shown that

$$\mathcal{E}[n_{SU_x}^{(m)} n_{SU_y}^{(n)}] = 0 \qquad x,y \in \{Se,.w,cs,cc\}; \; x \neq y \tag{1'(a)}$$
$$m,n \in \{1, \; 3, ..., L\}$$

$$\mathcal{E}[n_{SU_x}^{(m)} n_{SU_x}^{(n)}] = 0 \qquad x \in \{Se,.u,cs,m\}; \tag{17b}$$
$$m,n \in \{1,3,...,L\}; \; m \neq n$$

where $\mathcal{E}[X]$ denotes the expected Value' of $X >$ and 1, is the highest harmonic present at A/D outpu t.

Another approach to baseband recording of the received signal is shown in Fig. 2b. Unlike the previous recording scheme which uses the two-stage downconversion technique, this scheme records each subcarrier harmonic by directly downconverting it to baseband. As sl own in Fig. 2b, the sampled IF signal is still distributed into $(4n + 2)$ channels. The two channels used for recording the residual carrier remain the same for this new scheme. Consequently, the recorded carrier is as given by (1%) and (13b). 1 lowever, the subcarrier

harmonics are recorded at baseband by directly downconverting the upper and lower sidebands of each harmonic from W to baseband. That is, the mth subcarrier requires mixing the A/D output by $\sin[\hat{\Psi}_c + m\hat{\Psi}_{su}]$ and $\cos[\hat{\Psi}_c + m\hat{\Psi}_{su}]$ to record the upper sideband, and by $\sin[\hat{\Psi}_c - m\hat{\Psi}_{su}]$ and $\cos[\hat{\Psi}_c - m\hat{\Psi}_{su}]$ to record the lower sideband. As in the previous recording technique, this downconversion scheme also requires that a integer phase relationship be maintained between the subcarrier harmonics.

Following the same procedure as in the derivation of (5a)-(5d) [6], the recorded signals for this scheme can be shown to be (m is an odd integer)

$$SU_{s+}^{(m)} = \sqrt{P_{d}} \frac{2d}{\pi m} \cos[\Theta_c + m\Theta_{su}] + n_{SU_{s+}}^{(m)} \tag{18a}$$

$$SU_{s-}^{(m)} = -\sqrt{P_{d}} \frac{2d}{\pi m} \cos[\Theta_c - m\Theta_{su}] + n_{SU_{s-}}^{(m)} \tag{18b}$$

$$SU_{c+}^{(m)} = \sqrt{P_{d}} \frac{2d}{\pi m} \sin[\Theta_c + m\Theta_{su}] + n_{SU_{c+}}^{(m)} \tag{18c}$$

$$SU_{c-}^{(m)} = -\sqrt{P_{d}} \frac{2d}{\pi m} \sin[\Theta_c - m\Theta_{su}] + n_{SU_{c-}}^{(m)} \tag{18d}$$

where the subscripts, '+' and '-', respectively denote the upper and lower sidebands. The noises $n_{SU_{s+}}^{(m)}$, $n_{SU_{s-}}^{(m)}$, $n_{SU_{c+}}^{(m)}$, and $n_{SU_{s+}}^{(m)}$, can be shown to have a flat one-sided PSD level equal to N_0 within B_{su} z, the one-sided bandwidth of the low-pass filter $H_{su}(z)$ in Fig. 2b. These upper and lower sideband noises are correlated with respect to each other because the recorded signals of the direct recording scheme are correlated. Specifically, using (15a)-(15d) the signals in (18a)-(18d) can be rewritten as

$$SU_{s+}^{(m)} = SU_{sc}^{(m)} + SU_{cs}^{(m)} \tag{19a}$$

$$SU_{s-}^{(m)} = SU_{sc}^{(m)} - SU_{cs}^{(m)} \tag{19b}$$

$$SU_{c+}^{(m)} = SU_{cc}^{(m)} - SU_{ss}^{(m)} \tag{19c}$$

$$SU_{c-}^{(m)} = SU_{cc}^{(m)} - SU_{ss}^{(m)} \tag{19d}$$

Consequently,

$$n_{SU_{s+}}^{(m)} = n_{SU_{sc}}^{(m)} + n_{SU_{cs}}^{(m)} \tag{20a}$$

11

$$n_{SU_{s-}}^{(m)} = n_{SU_{sc}}^{(m)} - n_{SSU_{cs}}^{(m)}$$ (20b)

$$n_{SU_{c+}}^{(m)} = n_{SU_{cc}}^{(m)} - n_{SU_{ss}}^{(m)}$$ (20c)

$$n_{SU_{c-}}^{(m)} = n_{SU_{cc}}^{(m)} - 1 \, n_{SU_{ss}}^{(m)}$$ (20d)

Clearly, $n_{SU_{s+}}^{(m)}$ is correlated With $n_{SU_{s-}}^{(c)}$ and $n_{SU_{c+}}^{(m)}$ is correlated with $n_{SU_{c-}}^{(m)}$.

4   Coherent Baseband Demodulation

This section considers the coherent baseband demodulation of the carrier, and subcarrier when the modulation index (A in (1)) is such that the received signal consists of a sinusoidal carrier and squam-wave subcarrier; as well as, the case when the received signal consists of a suppressed carrier with square-wave subcarrier (i.e., A $= 90°$). The demodulation functions begin by reading the recorded signals of section 3 from a tape drive and then processing them to obtain control signals for the carrier, subcarrier, and suppressed carrier tracking loops. Recall that two methods for baseband recording of the 11 " signal were considered in section 3. It will be shown that the baseband processing, corresponding to these two methods is very similar except for a little extra processing that is required for the direct downconversion scheme, the second recording scheme in section 3. In this section, the carrier tracking loop, which is the same for both recording schemes, is described first. Then, the subcarrier and suppressed carrier loops for the two-stage downconversion recording scheme are described, and followed by the additional processing needed for using the signals of the direct downconversion scheme.

The carrier tracking loop, depicted near the bottom of Fig. 3a, respectively mixes the signals C_c and C_s with $\cos(\hat{\Theta}_c)$ and $\sin(\Theta_c)$ before subtracting the mixer outputs and accu - mulating the resulting samples over the loop update interval to form the carrier loop control Signal, V_q. Hence,

$$V_q(n) = \frac{1}{M_1} \sum_{k=nM_1}^{(n+1)M_1-1} [C_c(kT_s)\cos(\hat{\Theta}_c(kT_s)) - C_s(kT_s)\sin(\hat{\Theta}_c(kT_s))]$$ (21)

12

where $\hat{\Theta}_c$ is an estimate of the recorded carrier phase Θ_c. Substituting (13a) and (13L) for C_s and C_c, then expanding and canceling common terms, and assuming that the carrier phase error, $\phi_c \stackrel{\triangle}{=} \Theta_c - \hat{\Theta}_c$, varies slowly over the loop update interval, $T_u = M_1 T_s$, yields

$$V_q = \sqrt{P_c} \sin(\phi_c) + n_{V_q} \tag{22}$$

where

$$n_{V_q}(n) = \frac{1}{M_1} \sum_{k=nM_1}^{(n+1)M_1-1} [n_{c_c}(kT_s)\cos(\hat{\Theta}_c(kT_s)) - n_{c_s}(kT_s)\sin(\hat{\Theta}_c(kT_s))] \tag{23}$$

and n_{c_s} and n_{c_c} are given by (14a) and (14b). Since both n_{c_s} and n_{c_c} are zero mean with a flat one-sided PSD level equal to A^r_0 W/Hz within a much wider recording bandwidth B_c compared to $1/T_u$, it can be shown that n_{V_q} is Gaussian with zero mean and variance $N_0/2T_u$. Comparing *(22)* with (6) indicates that both the baseband carrier loop and the IF carrier loop have the same control signal in terms of signal power and noise variance. As a result, the carrier tracking variance of the baseband loop will be the same as a phase-locked 100]) tuned to the IF.

Recall that the squal-c-wave subcarrier was recorded at baseband by individually mixing each of its harmonics down to baseband and then recording each harmonic separately. For each subcarrier harmonic retained, four baseband signals given by (15a)-(15d) were actually recorded. As shown in Fig. 3a, each harmonic of the subcarrier is first read from the tape recorder and demodulated individually) and then properly weighted and summed to reconstruct the proper in-phase and quadrature samples for the various Costas loops. The demodulation procedures require the four recorded signals of each subcarrier harmonic being multiplied by the estimated carrier references, $\sin(\hat{\Theta}_c)$ and $\cos(\hat{\Theta}_c)$, and the estimated subcarrier harmonic references, $\sin(m\hat{\Theta}_c)$ and $\cos(m\hat{\Theta}_c)$ where m is an odd integer depending on the subcarrier harmonic under consideration. As depicted in Fig. 3a, the resulting signals are either added or subtracted to retain terms at $\Theta_c - \hat{\Theta}_c$ and $m(\Theta_{su} - \hat{\Theta}_{su})$, and eliminate terms at $\Theta_c + \hat{\Theta}_c$ and $m(\Theta_{su} + \hat{\Theta}_{su})$. The details of these demodulation procedures are provided in the Appendix A of [6]. Each of the demodulated signals of a particular subcarrier

13

harmonic is then properly weighted and summed to reconstruct the desired control signals for various tracking loops. For example, in the subcarrier loop depicted 011 the top half of Fig. 3a, the mth harmonic are sca ^{cc}] by $\frac{4}{m\pi}$ 011 the in-phase arm, and $\frac{4}{m\pi}\sin(\frac{m}{2}\pi W_{su})$ on the quadrature arm (W_{su} is the subcarrier window sire). Subsequently, the scaled in-phase signals corresponding to each harmonic are added to form the input to the in-phase syn n-Lo] accumulator whereas, the scaled quadrature signals are added to form the input to the quadrature symbol accumulator. The product of the in-phase accumulator output, Y_i in Fig. 3a, and the quadrature accumulator output, $Y_{q,su}$ in Fig. 3a, is the subcarrier loop control signal. The symbol accumulator outputs corresponding to the lth symbol are given as [(i]

$$Y_i = \sqrt{P_d}a_l\cos(\phi_c)\frac{8}{\pi^2}\sum_{\substack{j=1\\j\,odd}}^{L}\left(\frac{1}{j^2}\cos(j\phi_{su})\right) + n_{Y_i} \tag{24}$$

and

$$Y_{q,su} = \sqrt{P_d}a_l\cos(\phi_c)\frac{8}{\pi^2}\sum_{\substack{j=1\\j\,odd}}^{L}(\frac{\sin(\frac{j}{2}\pi W_{su})}{j^2}\sin(j\phi_{su})) + n_{Y_{q,su}} \tag{25}$$

where the independent noise tern is, n_{Y_i} and $n_{Y_{q,su}}$, are shown in Appendix A of [6] to have variance $N_0/(2T)$ and $N_0 W_{su}/(2T)$, respectively, as L approaches infinity in the above two equations. That is, for sufficiently large L, the noise variances of n_{Y_i} and $n_{Y_{q,su}}$ are approximately the same as the variances of n_{Z_i} and $n_{Z_{q,su}}$ in (7) and (8), respectively. Furthermore, the signal part of (24) and ('l), and (25) and (8) are also equal as L approaches infinity. This can be easily shown by using the Fourier series expansion of $F_I(\phi_{su})$ and $F_Q(\phi_{su})$ in (7) and (8) given as follows,

$$F_I(\phi_{su}) = \frac{8}{\pi^2}\sum_{\substack{j=1\\j\,odd}}^{\infty}\frac{1}{j^2}\cos(j\phi_{su}) \tag{26}$$

and

$$F_Q(\phi_{su}) = \frac{8}{\pi^2}\sum_{\substack{j=1\\j\,odd}}^{\infty}\frac{\sin(\frac{j}{2}\pi W_{su})}{j^2}\sin(j\phi_{su}) \tag{27}$$

As a result of the subcarrier loop accumulator outputs of the ARX and BTD being approximately equal for sufficiently large L, the control signals, $Y_i Y_{q,su}$ and $Z_i Z_{q,su}$, and tracking

variance of both loops can also be shown to be equal.

Next, let's consider the suppressed carrier with subcarrier loop also shown in Fig. 3a. As shown in the figure, it is a Costas loop sharing the same in-phase arm with the subcarrier Costas loop. Hence, the suppressed carrier in-phase accumulator output, Y_i, is as given in (24). The processing in the suppressed carrier loop quadrature arm is very similar to that of the subcarrier loop. Hence, following the same derivation as in the subcarrier loop quadrature arm, the suppressed carrier quadrature arm accumulation over the lth symbol can be shown to be

$$Y_{q,sca} = \sqrt{P_d} a_l \sin(\phi_c) \frac{8}{\pi^2} \sum_{\substack{j=1 \\ j \, odd}}^{L} \frac{1}{j^2} \cos(j\phi_{su}) + n_{Y_{q,sca}} \qquad (28)$$

As before, the equivalence of the suppressed carrier loops of the BTD and ARX is established by comparing the in-phase and quadrature accumulator outputs of both loops. The equivalence of the in-phase arms has already been shown earlier. The signal part of the quadrature arm accumulations given by (1 2) and (28) are seen to be equivalent after letting L go to infinity in (28) and then using (26) for the infinite sum. The noise part of (12) and (28), as L approaches infinity in (28), can also be shown to have the same variance (Are/27'), Furthermore, it can be shown that n_{Y_i}, and $n_{Y_{q,sca}}$ are uncorrelated to each other.

The equivalence of the ARX and BTD loops has been shown as L approaches infinity. Now consider the case when the input to these loops is bandlimited so that the subcarrier is no longer a square-wave That is, consider the case when L in (4) is small. In this case, the ARX and BTD loops are not expected to have identical performance, mainly because the ARX is designed to be optimum for a square-wave subcarrier. The performance of both subcarrier loops for a finite number of harmonics at the input is currently under investigation. The ARX performance is being quantified for both an unfiltered and filtered square-wave reference signal. Relative to the case when both the input and reference signals are perfect square-waves, the first case (filtered input, unfiltered reference) is expected to have degraded performance because the reference is no longer "matched" to the input. The filtered input,

15

filtered reference case is expected to be better than case one but worse than the BTD loop), which also uses a filtered square-wave reference. One might immediately wonder why the second case is expected to be worse than the $11'1'1$) when both use filtered references. The main reason is that ARX directly mixes the filtered reference with the filtered input which gives rise to cross-products at the mixer output whereas, the BTD eliminates cross-products by individually mixing the filtered signals one harmonic at a time.

Finally, consider the coherent baseband demodulation of the signals that were recorded as a result of the direct downconversion scheme, the second recording scheme described in section 3. As indicated earlier, the demodulator for the direct scheme is very similar to the two-stage downconversion scheme demodulator except that the former requires a little extra processing. Specifically, the recorded signals for the direct scheme, given by (1 8a)- (1 8d), are combined to yield the signals $SU_{ss}^{(m)}$, $SU_{sc}^{(m)}$, $SU_{cs}^{(m)}$ and $SU_{cc}^{(m)}$ which were the input signals to the two-stage demodulator described in this section. From (29)-(32), it is clear that the input signals to the two-stage demodulator can be generated by using two adders and two subtractors (per harmonic) on the signals $SU_{s+}^{(m)}$, $SU_{s-}^{(m)}$, $SU_{c+}^{(m)}$, and $SU_{c-}^{(m)}$. After these additions and subtractions, shown in Fig. 3b, the rest of the signal processing remains the same as the previous scheme.

5 Requirements **for Software 1** mplementation of the BTD

As indicated earlier, the BTD depicted in Fig. 3a is targeted for implementation on a general purpose engineering workstation. The primary concern with a software implementation is whether a general purpose workstation can provide the computational speed required for real time processing of the recorded signals. For example, if the received symbol rate is 1 K symbols/sec and the A/D sampling rate is 101{ sallqdcs/see, then a real time demodulator would process 1 OK samples/sec and detect 11{ sylnt~ols/see, This section first determines

the computational speed required (in o]maticJns/sex) for implementing the BTD in real time when the symbol rate is 1 K symbols/sec and the sample rate is 1 OK samples/sec. Next, it determines the feasibility of implementing the BTD on a Sun Sparc 2 and Sun Sparc 10 workstation.

R ccall **that** the two modes for the BTD are the residual carrier with subcarrier mode (A =/ 90°) and the suppressed carrier with subcarrier mode (Δ = **900).** The number of (acl-dition and multiplication) operations/sec, for a given mode, can be computed by separately counting the operations/sample and operations/symbol in Fig. 3a and then multiplying by the operations at the sampling rate and the operations at the symbol rate. Mathemati cally,

$$\text{ops} , \left(\frac{\text{(no. of `+ ` and `x')} \text{ ops}}{\text{sample}}\right)\left(\frac{10K \text{ samples}}{\text{sec}}\right) - \left(\frac{\text{(no. of `+ ` and `x')} \text{ ops}}{\text{symbol}}\right)\left(\frac{1K \text{ symbols}}{\text{sec}}\right)$$

(29)

where the sample and symbol (floating point) operations for the coherent demodulator in Fig. 3a are tabulated in Table 2. Both addition and multiplication have been counted as 1 operation each. Furthermore, the look-up table operations are at the sample rate since the look-up table is considered to be part of the carrier and subcarrier NCOs. The coherent demodulator for the direct downconversion scheme needs four 1 nore sample operations per harmonic, as shown in Fig. 3b, and is not considered separately. With the number of harmonics, n, equal 3 (i.e., the 1st, 3rd, and 5th harmonics recorded) in Table 2, there are 71 operations/sample and 48 operations/symbol for the residual carrier mode, and there are 98 operations/sample ant] 39 operations/symbol in the suppressed carrier mode. Consequently, at 1 Ksps and 10 KHz sampling rate, a real time processor would be required to provide 758K ops and 1019K ops for the residual carrier and suppressed carrier modes, respectively. Table **3** lists the throughput utilized by a software implementation of the BTD for various computers. Throughput, measured in symbols/sec, is defined as the computers total capacity for work. In Table 3, the percent throughput (at IOK sampling rate and 1K symbol rate) utilized by a Sun SS-2 was obtained by simulating a portion of the BTD on the Sun SS-

17

2 and then linearly extrapolating the results to determine the throughput utilization for a software implementation of the entire BTD). The throughput of the remaining computers were obtained by linearly extrapolating the Sun SS-2 results using the Specfp92 benchmark. A Specfp92 rating of a computer, obtained by running a collection of commonly used programs on a target system, is a ~m!a.sure of its performance relative to a VA X-1 1/780. For example, the Sun *SS-2* is expected to perform *22.8* times better than a VAX-11 /780 since its Specfp92 rating is 22.8. It is clear from Table 3 that several computers will be able to process the recorded data in real time.

6 Post-Processing Strategies

Post-processing is one of the key features of the BTD as it allows the BTD to recover data lost during acquisition, and resynchronization. Since the received signal is recorded, the BTD can use different configurations (e.g. different loop bandwidths) to process the signal and obtain better performance. A more sophisticated strategy relies on "smoothing" to use information obtained from the signal after it has been acquired to go back in time and use the extracted *a priori* information intelligently. Specifically, Kalman filters or IJCast-Squares estimators [7] can be used to process the data backwards where the signal state is formulated using the phase, frequency, and/or frequency rate of the incoming signal after acquisition and the covariance matrices are initialized with the appropriate tracking jitters. Another approach relies entirely on the information contained in the state-s}hacx representation of the loop filter. Depending on its order, the filter contains information on the frequency and possibly frequency rate of the signal. By playing the data backwards, the frequency rate is reversed in sign and by adjusting the appropriate states of the loop filter, the phase locked loop can be made to go back in time while starting in lock. All these techniques are currently being investigated and their respective performances assessed.

Preliminary work, however, on processing and reprocessing recorded samples of the down-

link carrier has been performed [5] where an adaptive carrier loop bandwidth selection algorithm is used for reprocessing recorded samples of the downlink carrier from the Galileo spacecraft. Consider Fig. 4 (reprinted from [5]) which shows the loop bandwidth required to track the Galileo downlink carrier as a function of elapsed time. The track begins by setting the carrier phase-locked loop (1'1,1,) to an initial loop bandwidth B_0. For example, consider the solid line in Fig. 4 which corresponds to B_0 =- 0.1 Hz. In this case, all the recorded samples are initially tracked with a loop bandwidth of 0.1 Hz and the times at which the loop loses lock are recorded. Samples lost during the out-of-lock state are recovered by backward processing of the samples. The bandwidths used for backward processing are indicated by the "spikes" in Fig. 4.

'7 Conclusion

This article presented the Buffered Telemetry Demodulator (11'1'1), a software receiver that is suitable for low cost space missions characterized by low data rates, and relatively weak downlinks. The first application of the BTD will be the NASA's Galileo S-Band Mission where the symbol rate will range from 32 sps to 512 sps and the symbol SNR will be as low as -10 dB. In scenarios such as Galileo where the link margin is very low, tracking loops not only take an unusually long time to acquire but often slip cycles. The main advantage that the BTD has over existing deep space receivers is that once acquisition) occurs, it can use estimates of the signal state (such I as frequency, phase, and doppler rate) to basically go back in time and recover those symbols lost during acquisition, resynchronization, and cycle slips. Furthermore, since the proposed recording schemes individually record each subcarrier harmonic, the BTD can be easily implemented on several general purpose workstations.

Glossary

Ψ_c incoming Carrier Phase

$\hat{\Psi}_c$ Predicted Carrier Phase

Θ_c Carrier Phase Offset = $\Psi_c - \hat{\Psi}_c$

$\hat{\Theta}_c$ Carrier Phase Offset Estimate

ϕ_c Carrier Phase offset Error = $\Theta_c - \hat{\Theta}_c$

Ψ_{su} incoming Subcarrier Phase

$\hat{\Psi}_{su}$ Predicted Subcarrier Phase

Θ_{su} Subcarrier Phase Offset = $\Psi_{su} - \hat{\Psi}_{su}$

$\hat{\Theta}_{su}$ Subcarrier Phase Offset Estimate

ϕ_{su} Subcarrier Phase Offset Error = $\Theta_{su} - \hat{\Theta}_{su}$

$XSU_{ss}^{(m)}$ m^{th} subcarrier harmonic, derived from mixing the received signal with $\sqrt{2}\sin(\hat{\Psi}_c)\sin(m\hat{\Psi}_{su})$

$SU_{ss}^{(m)}$ the low-pass filtered version of $XSU_{ss}^{(m)}$

$XSU_{sc}^{(m)}$ m^{th} subcarrier harmonic, derived from mixing the received signal with $\sqrt{2}\sin(\hat{\Psi}_c)\cos(m\hat{\Psi}_{su})$

$SU_{sc}^{(m)}$ the low-pass filtered version of $XSU_{sc}^{(m)}$

$XSU_{cs}^{(m)}$ m^{th} subcarrier harmonic, derived from mixing the received signal with $\sqrt{2}\cos(\hat{\Psi}_c)\sin(m\hat{\Psi}_{su})$

$SU_{cs}^{(m)}$ the low-pass filtered version of $XSU_{cs}^{(m)}$

$XSU_{cc}^{(m)}$ m^{th} subcarrier harmonic, derived from mixing the received signal with $\sqrt{2}\cos(\hat{\Psi}_c)\cos(m\hat{\Psi}_{su})$

$SU_{cc}^{(m)}$ the low-pass filtered version of $XSU_{cc}^{(m)}$

$XSU_{s+}^{(m)}$ m^{th} subcarrier harmonic, derived from mixing the received signal with $\sqrt{2}\sin(\hat{\Psi}_c + m\hat{\Psi}_{su})$

$SU_{s+}^{(m)}$ the low-pass filtered version of $XSU_{s+}^{(m)}$

$XSU_{s-}^{(m)}$ m^{th} subcarrier harmonic, derived from mixing the received signal with $\sqrt{2}\sin(\hat{\Psi}_c - m\hat{\Psi}_{su})$

$SU_{s-}^{(m)}$ the low-pass filtered version of $XSU_{s-}^{(m)}$

$XSU_{c+}^{(m)}$ m^{th} subcarrier harmonic, derived from mixing the received signal with $\sqrt{2}\cos(\hat{\Psi}_c + m\hat{\Psi}_{su})$

$SU_{c+}^{(m)}$ the low-pass filtered version of $XSU_{c+}^{(m)}$

$XSU_{c-}^{(m)}$ m^{th} subcarrier harmonic, derived from mixing the received signal with $\sqrt{2}\cos(\hat{\Psi}_c - m\hat{\Psi}_{su})$

$SU_{c-}^{(m)}$ the low-pass filtered version of $XSU_{c-}^{(m)}$

References

J. S. Hinedi, "NASA's Next Generation All-Digital Deep Space Network Breadboard Receiver," *IEEE Trans. on Commun.*, w]. 4 1 , pp. 246-257, Jan. 1993.

2. J. H. Yuen, *"Deep Space Telecommunications Systems Engineering,"* Plenum Press, New York, 1983.

3. W. J. Hurd and S. Acquirre, "A Method to 1)ramatically Improve Subcarrier Tracking," *IEEE Trans. on Commun.* , vol.36, pp.238-243, February 1988.

4. A. Mileant and S. Hinedi, "overview of Arraying Techniques for Deep Space Communications," to be published in *IEEE Trans. Commun.*

5. D. A. Watola, "Adaptive Low-Bandwidth Tracking of Galileo and Pioneer 10 Carriers,'' *TDA Progress Report 42- 111*, Jet Propulsion Laboratory, Pasadena, California, pp. 167-178, November 1992.

(i. 11. Tsou, B. Shah, R. Lee, and S. Hinedi, ''A Functional Description of the Buffered Telemetry Demodulator," *TDA Progress Report 1.2-112*, Jet Propulsion Laboratory, Pasadena, California, pp. 50-73, February, 1993.

?. 11.11. Anderson and J. B. Moore, *Optimal Filtering*, Prentice-Hall, Englewood Cliffs, NJ, 1979.

Table Ia, Loss in data power as a function of subcarrier harmonics.

Table Ib, Loss in data power due to ideal low-pass filtering of data.

Highest recorded subcarrier harmonic, L	Number of subcarrier harmonics at A/I output, n	Loss, dB	$B_{su}T$	Loss, dB
1	1	0.91	1	0.44
3	2	0,45	2	0.22
5	3	0.30	3	0.15
7	4	0.22	4	0.11
9	5	0.18	5	0.09

Table 2. Required number of operations for the demodulation function (*n is the number of harmonics recorded),*

Mode	Multiplication operations per sample	Multiplication operations per symbol	Addition operations per sample	Addition operations per symbol	Lookup table
Residual carrier with subcarrier	$6 + 8n$	14	$13 + 6n$	24	$4 + 2n$
Suppressed carrier with subcarrier	$4 + 14n$	14	$12 + 10n$	25	$4 + 2n$
Suppressed carrier with no subcarrier	6	12	10	17	4

Table 3. Throughput comparison (*n is the number of harmonics recorded).*

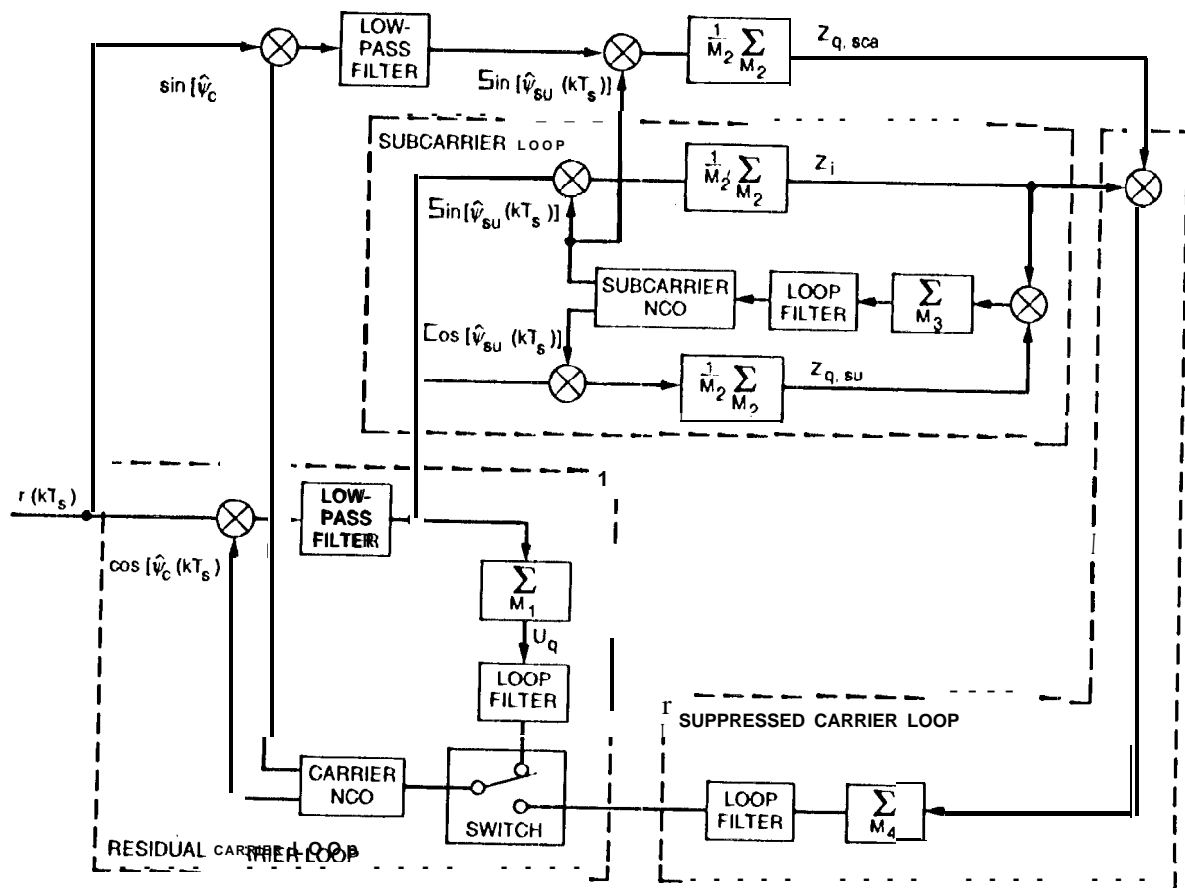| System	SPECfp92	Percent throughput utilized ($n = 3$)	Percent throughput utilized ($n = 5$)
Sun SS-2	22.8	100	151
sun SS-10/30	52.9	43	65
sun SS-10/41	64.7	35	53
Sun SS-10/52	71.4/CPU	32 (on one CPU)	48 (on one CPU)
SGI Crimson	63.4	36	54
HP 710	47.6	48	72
HP 750	75.0	30	45
IBM 34o	51.9	44	66
IBM 560	85.6	27	41
Intel Xpress (486)	14.0	160	242

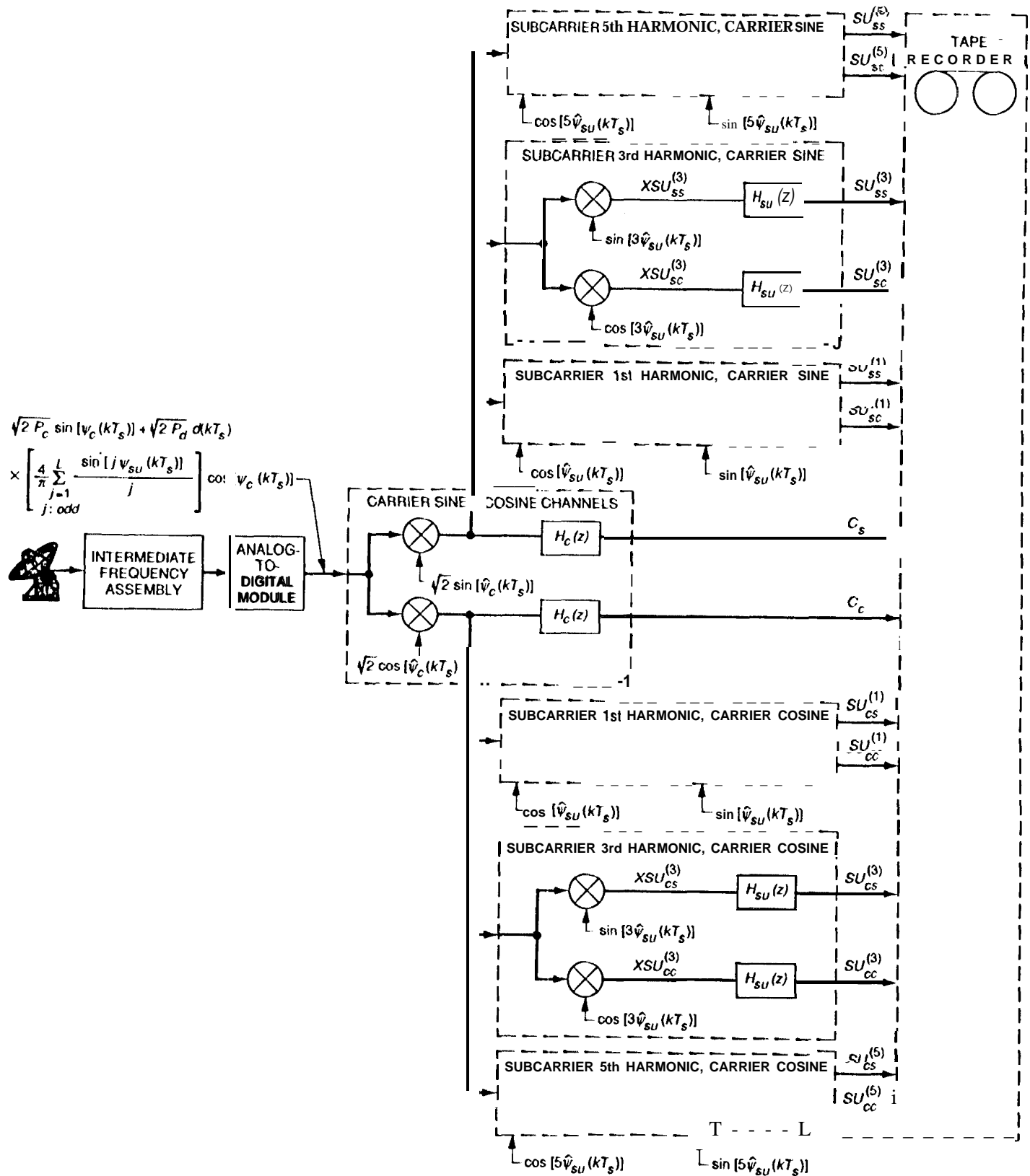Fig. 1. A simplified block diagram of the ARX IL

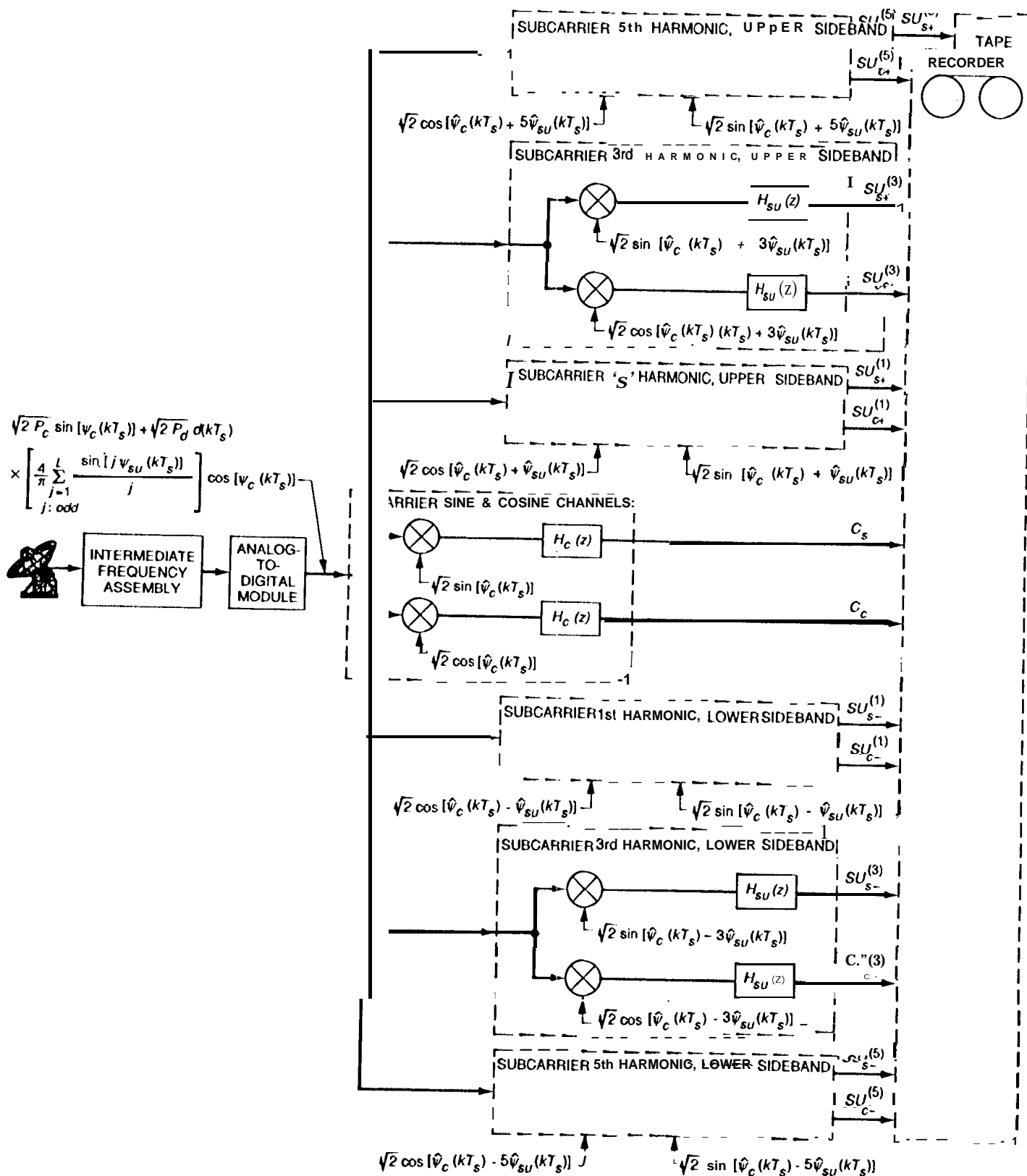Fig. 2a. The two-stage downconversion recording scheme,
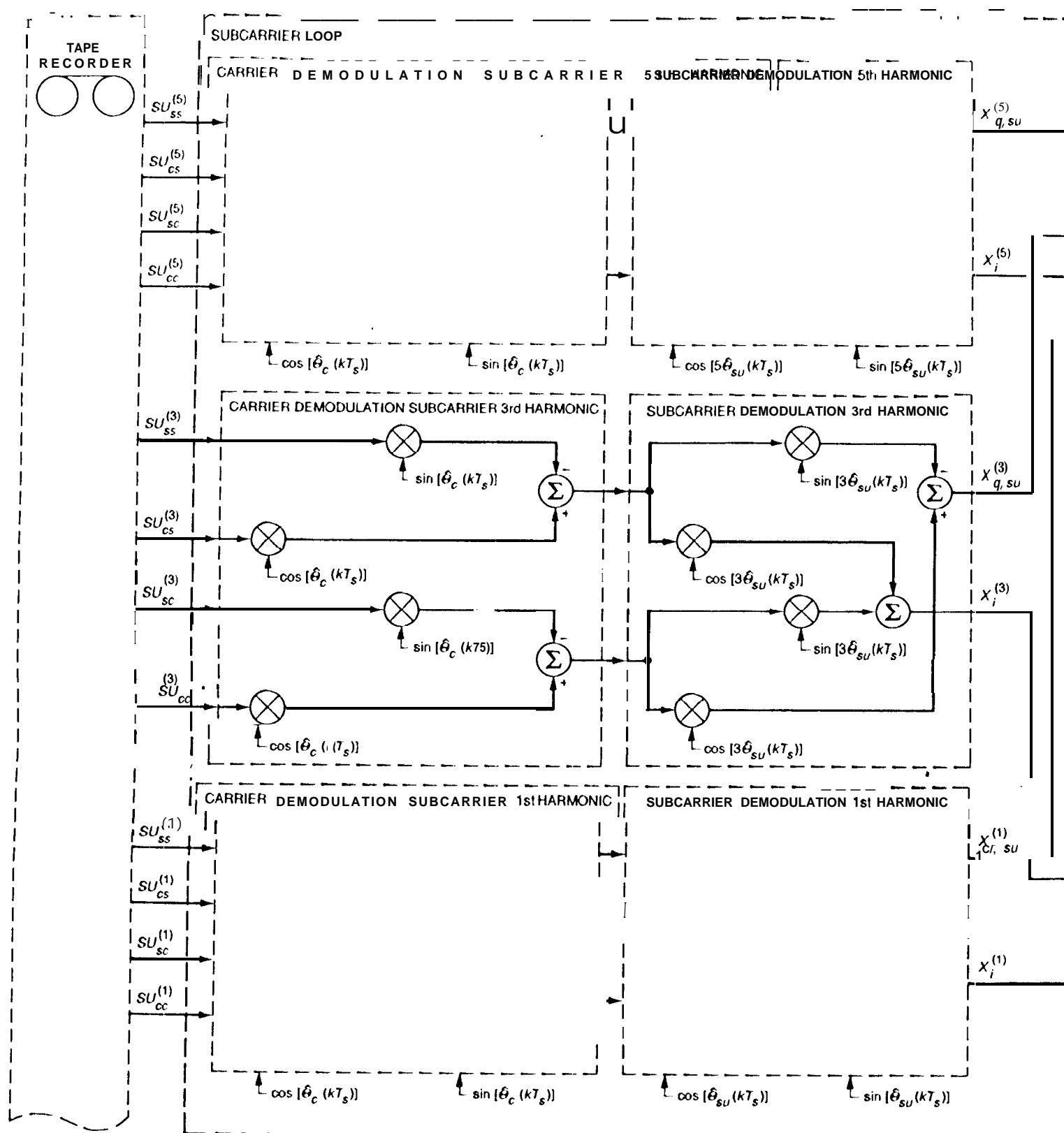
Fig. 2b. The direct downconversion recording scheme.

Figure 3a, Part 1

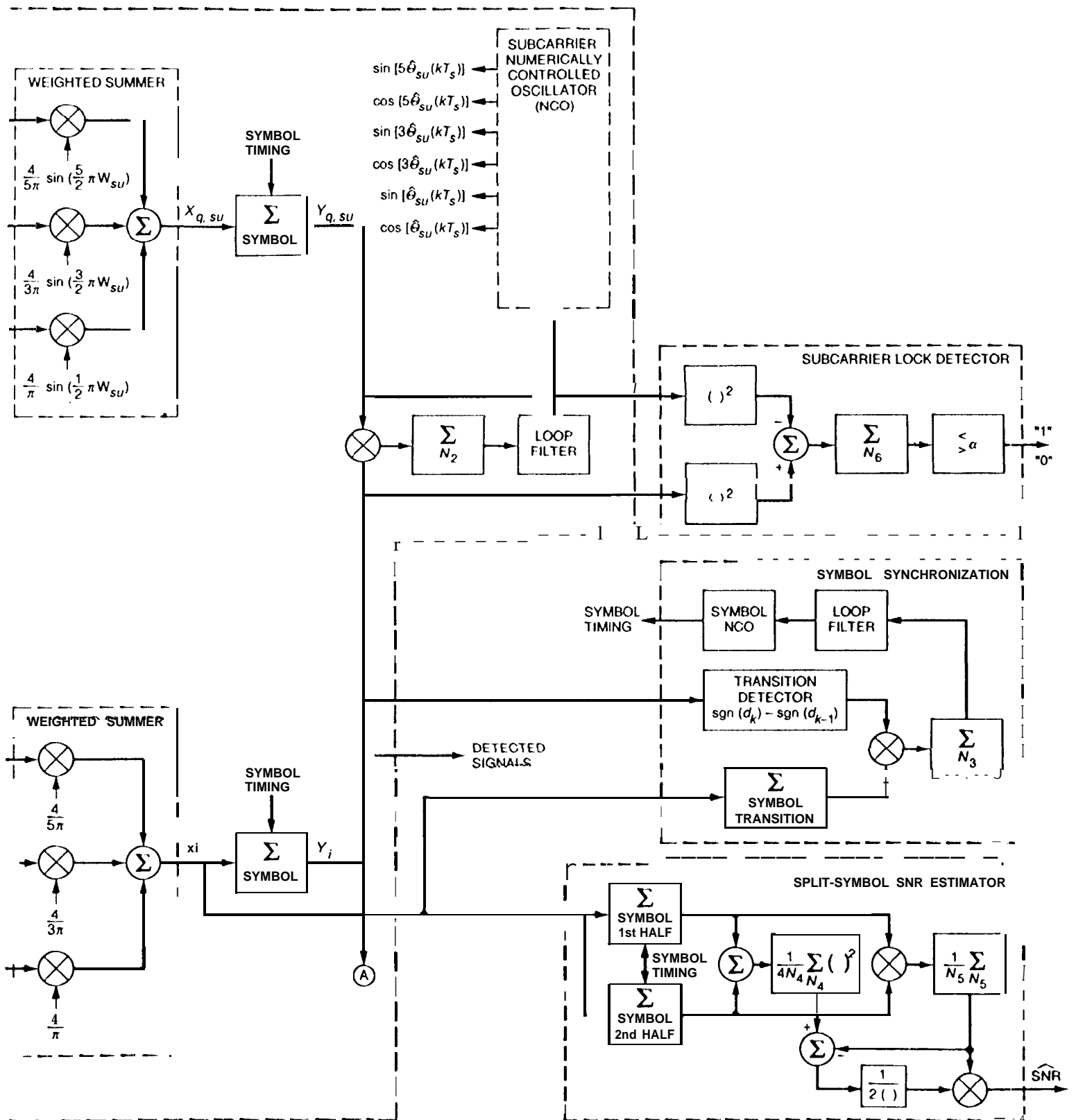Fig. 3a. The coherent baseband demodulator for the two-stage recording scheme.
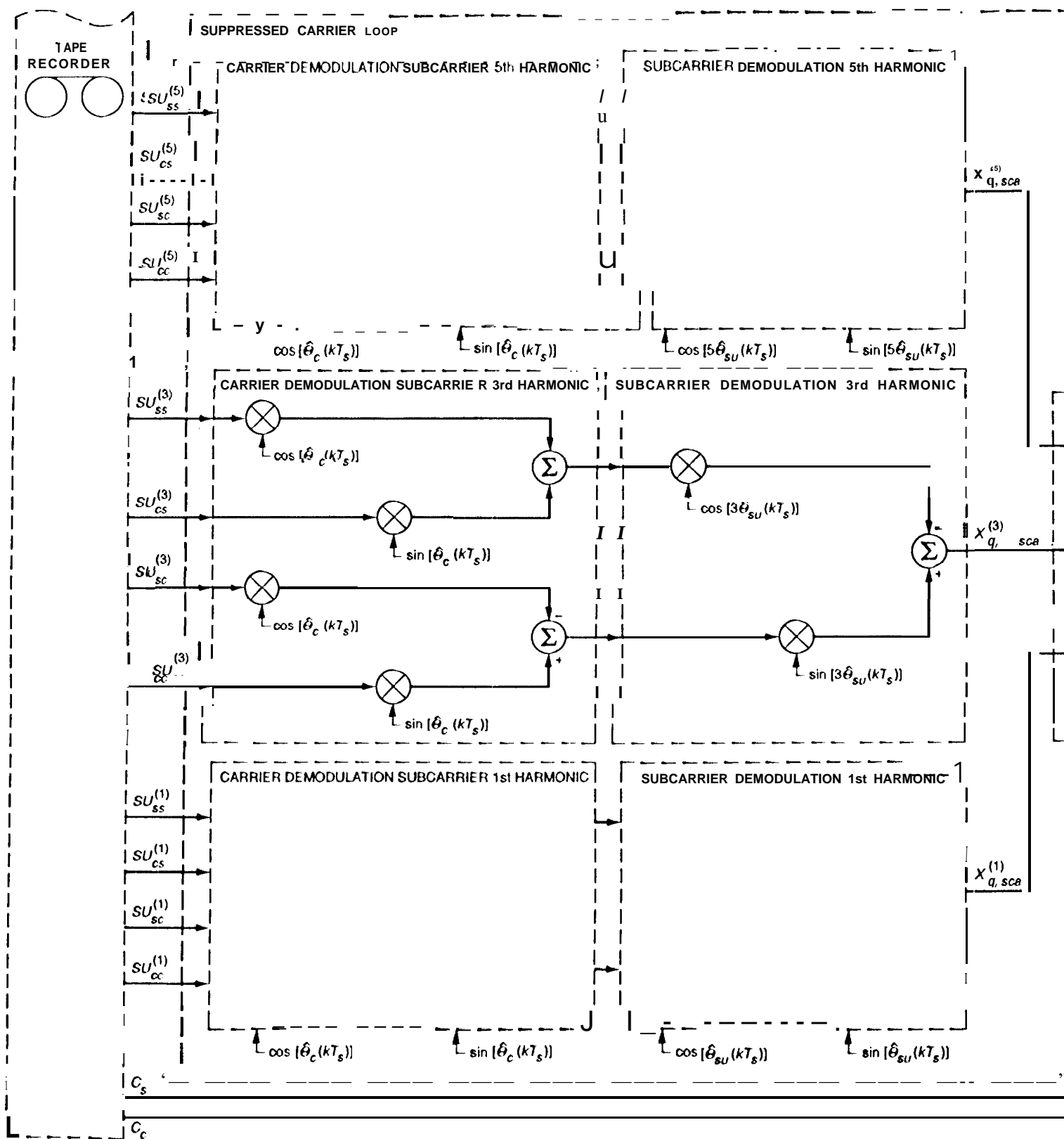
Figure 3a. Part 2

Fig. 38. (contd).

WEIGHTED SUMMER

$\frac{4}{5\pi}$

$\frac{4}{3\pi}$

$\frac{4}{n}$

$\Sigma\Sigma$

$X_{q, sca}$

SYMBOL
TIMING

$\sum_{SYMBOL}$

$Y_{q, sca}$

THIS INPHASE ARM IS SHARED
WITH THE SUBCARRIER 100P
[SEE PRECEDING PAGE)

$\sum_{N_2}$

LOOP
FILTER

CARRIER TRACKING LOOP

$\sin [\hat{\theta}_c (kT_s)]$

$\cos [\hat{\theta}_c (kT_s)]$

Σ

$\sum_{M_1}$

V_q

LOOP
FILTER

$\sin [\hat{\theta}_c (kT_s)]$

$\cos [\hat{\theta}_c (kT_s)]$

CARRIER
NCO

RESIDUAL
CARRIER

SUPPRESSED
CARRIER

CARRIER LOCK DETECTOR

$\sin [\hat{\theta}_c (kT_s)]$

$t \cos [\hat{\theta}_c (kT_s)]$

Σ

$\frac{1}{N_7} \sum_{N_7}$

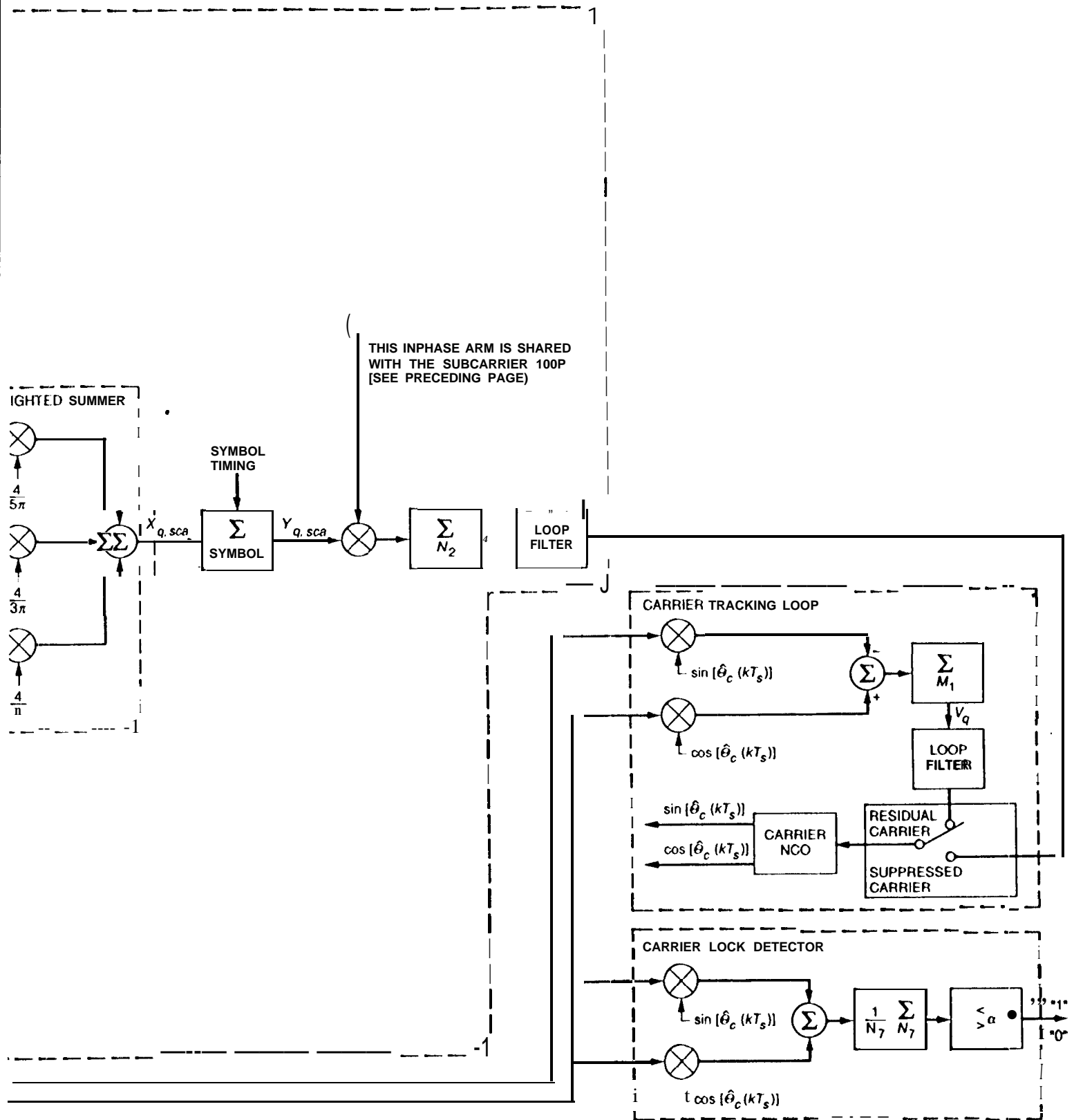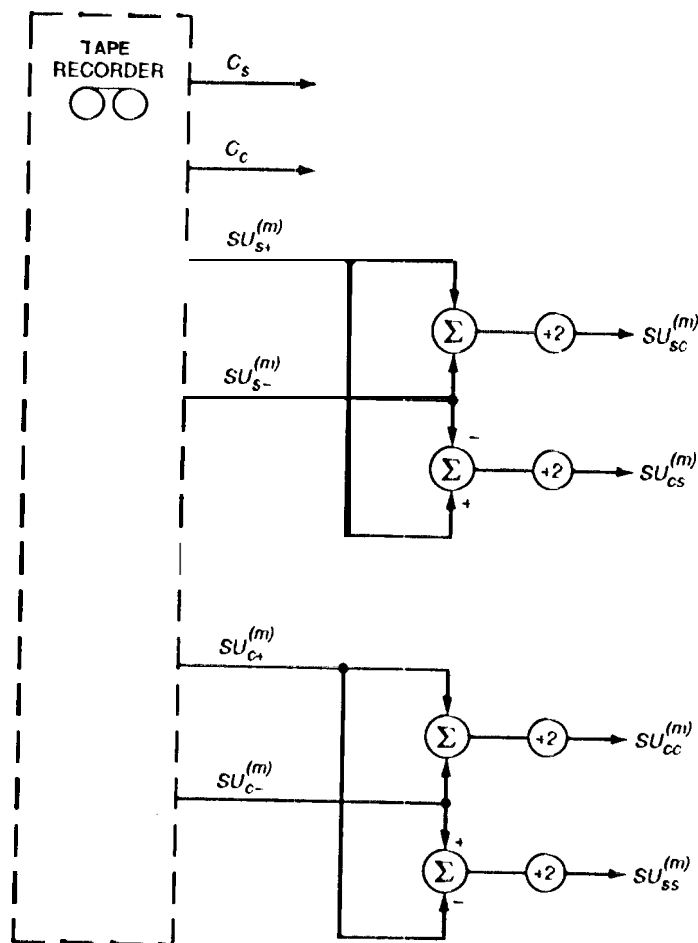$\begin{smallmatrix} < \\ > \end{smallmatrix} \alpha$

"1"

"0"

Figure 3a. Part 4

Fig. 3b. The processing required 10 generate the signals $SU_{ss}^{(m)}$, $SU_{sc}^{(m)}$, $SU_{cs}^{(m)}$, $SU_{cc}^{(m)}$ from the signals $SU_{s+}^{(m)}$, $SU_{s-}^{(m)}$, $SU_{c+}^{(m)}$, and Sip.
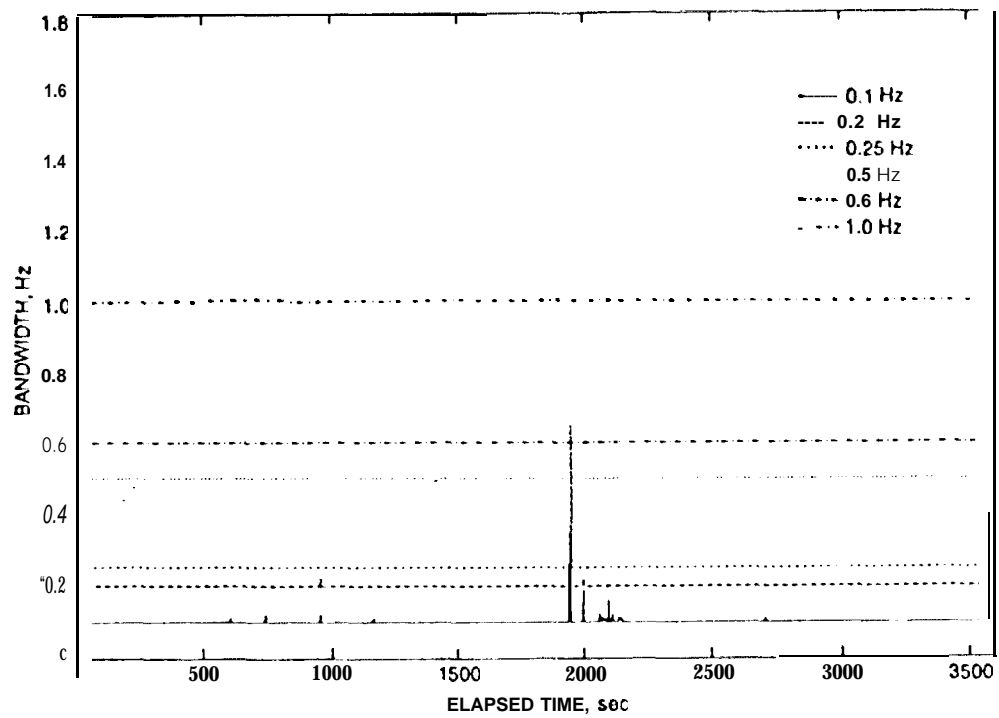
Fig. 4. Loop bandwidth for Galileo carrier phase recovery at various B_0. The events near ~3570 sac are due to a switch from one-way to two-way tracking (reprinted from [5])